Seeding of the forward Raman instability by ionization fronts and Raman backscatter

D. F. Gordon,[1] B. Hafizi,[2] P. Sprangle,[1] R. F. Hubbard,[1] J. R. Peñano,[3] and W. B. Mori[4]
[1]*Plasma Physics Division, Naval Research Laboratory, Washington, DC 20375*
[2]*Icarus Research, Inc., P.O. Box 30780, Bethesda, Maryland 20824-0780*
[3]*LET Corp., 4431 MacArthur Boulevard, Washington, DC 20007*
[4]*University of California, Los Angeles, Los Angeles, California 90095*
(Received 1 May 2001; revised manuscript received 28 June 2001; published 21 September 2001)

The self-modulated laser wakefield accelerator utilizes the forward Raman instability to drive a large-amplitude plasma wave. The effectiveness of this process could depend on how it competes with other processes such as self-focusing and cavitation, or other instabilities such as filamentation and hosing. The relative timing between the various processes is dependent on the nature of the seed for each instability. Both ionization fronts and Raman backscatter are capable of seeding the forward Raman instability. This causes the forward Raman instability to emerge much earlier than would otherwise be expected.

DOI: 10.1103/PhysRevE.64.046404 PACS number(s): 52.38.Bv, 52.38.Kd, 52.50.Jm, 52.65.Rr

I. INTRODUCTION

The self-modulated regime of laser plasma interactions is defined by a laser pulse with a normalized vector potential on the order of unity ($eA/mc^2 \approx 1$), a pulse length of several plasma periods ($c\tau_{\text{pulse}} \approx 10\lambda_p$), and a frequency several times the plasma frequency ($\omega_0 \approx 10\omega_p$). In the one-dimensional limit, the interaction between such a pulse and a plasma is dominated by the forward Raman instability [1]. The forward Raman instability results in a modulation of the laser pulse at the plasma frequency, and a corresponding modulation of the plasma density. The resulting plasma wave grows until it reaches the wave-breaking limit, after which large numbers of background electrons are self-trapped and accelerated to high energies. The self-modulated laser wakefield accelerator (SM-LWFA) utilizes this mechanism to generate a beam of high-energy electrons. These high-energy electrons have been observed both experimentally and in particle-in-cell (PIC) simulations [2–9].

In modeling the SM-LWFA, it has always been assumed that the plasma is preionized. In experiments, on the other hand, the plasma has always been created by the same laser pulse which is to undergo self-modulation. Moreover, in modeling the SM-LWFA certain reduced models are sometimes used which preclude Raman backscatter. In this paper we show that for typical experimental parameters, both ionization effects and Raman backscatter can strongly influence the evolution of the forward Raman instability.

The importance of ionization effects in the self-modulated regime follows from sensitivity to initial conditions. In particular, the evolution of the laser and the electron distribution function will depend strongly on the manner in which the various instabilities are seeded. In multidimensions, the set of possible outcomes is quite rich due to the fact that the plasma supports Raman scattering at all angles, along with filamentation and whole beam self-focusing. The one-dimensional case is much simpler, since only Raman forward scatter (RFS) and Raman backscatter (RBS) are important. In this paper we restrict our attention to the one-dimensional case. Although a one-dimensional study may not provide an adequate description of laboratory experiments, it does provide the background for future studies in multidimensions.

II. SEEDING MECHANISMS

Parametric instabilities in a plasma are seeded by density fluctuations, or fluctuations in the laser envelope, which contain Fourier components lying within the spectrum of unstable frequencies. In the case of Raman forward scattering (RFS) the obvious contributions to this seed are the wake driven by the finite laser pulse and the plasma oscillations comprising the thermal noise spectrum. A less obvious contribution is the wake driven by the ionization front, and more subtle still, is the coupling between RBS and RFS. The seeding of RFS via RBS has been discussed previously [10], and will be revisited in this paper. The possibility that RFS might be seeded by ionization fronts was alluded to in a theoretical context in Refs. [11] and [12], and in an experimental context in Ref. [13].

In the case of RBS, the instability grows from density fluctuations with frequency ω_p and wave number $\approx(2\omega_0 - \omega_p)/c$, where ω_p is the plasma frequency and ω_0 is the laser frequency [14]. Such fluctuations could emerge from thermal noise, or from nonlinear forces exerted by the laser itself. In the case of linearly polarized radiation, the $\mathbf{v}\times\mathbf{B}$ force contains a component with frequency $2\omega_0$ and wave number $2\omega_0/c$. The plasma responds to this force with a component not only at the driving frequency, but also at the natural frequency ω_p. The response at the natural frequency maintains the wave number of the driver and can therefore be amplified by RBS. This conclusion is corroborated by fluid simulations in which linearly polarized light excites RBS while circularly polarized light does not [15]. In PIC simulations, however, numerical noise levels are higher and RBS is therefore excited even for circular polarization.

III. IONIZATION-INDUCED WAKES

The laser intensities and time scales in typical SM-LWFA experiments lead to tunneling as the dominant ionization mechanism. We therefore model ionization using the Ammosov, Delone, and Krainov (ADK) model [16] for tunnel-

ing ionization. For hydrogen or helium, the rate at which electron density increases is

$$\frac{dn_e}{dt}=\sum_i 1.61\omega_a\frac{Z_i^2}{N_i^{9/2}}\left[10.87\frac{Z_i^3}{N_i^4}\frac{E_a}{E}\right]^{2N_i-3/2} \times\exp\left[-\frac{2}{3}\frac{Z_i^3}{N_i^3}\frac{E_a}{E}\right]n_i, \quad (1)$$

where the sum is over the neutral and ion particle species, E is the laser field, $\omega_a\approx 4.13\times 10^{16}\,\mathrm{s}^{-1}$, $E_a\approx 5.21\times 10^{11}$ V/m, Z_i is the residual charge state of species i, U_i is the ionization potential of species i normalized to that of hydrogen, $N_i=Z_iU_i^{-1/2}$, and n_i is the density of species i. The exponential in Eq. (1) leads to a threshold behavior whereby the ionization rate suddenly becomes very large when the laser intensity reaches a certain value. In laser ionized plasmas, this leads to a density profile which is well approximated by a step function moving with the laser. For typical SM-LWFA parameters, the ionization front occurs very early in the pulse.

In a preionized plasma, a weakly relativistic laser pulse drives a wake field according to [17]

$$\phi(\zeta)\approx\frac{1}{4}\int_0^\zeta |a(\zeta')|^2\sin(\zeta-\zeta')d\zeta', \quad (2)$$

where ϕ is the scalar potential normalized to mc^2/e, a is the envelope of the vector potential normalized to mc^2/e, and $\zeta=z-ct$. The complex envelope a is defined in terms of the real-valued vector potential as follows:

$$\tilde{a}=\frac{a}{2}e^{i\omega_0\zeta/c}+\text{c.c.}$$

Here, ω_0 is the frequency of the laser. For typical SM-LWFA parameters, the amplitude of the wakefield is such that $\phi\ll a$. However, the amplitude is still large enough so that the corresponding density fluctuation is expected to be the dominant seed for Raman instabilities in the forward or near-forward direction.

There are two mechanisms whereby an ionization front can enhance the wakefield described by Eq. (2). The first mechanism we call the ''ionization-induced ponderomotive force'' and the second we call ''ionization-induced steepening.'' The ionization-induced ponderomotive force was first described in Ref. [11], where it was shown that if a particle is born at rest in a plane wave, the ensuing orbit contains a transverse drift momentum

$$\langle p_\perp\rangle=q\tilde{a} \quad (3)$$

and a longitudinal drift momentum

$$\langle p_\parallel\rangle=\frac{q^2}{mc}\frac{a^2}{2}\begin{cases}1/2+\sin^2\psi & \text{linear polarization}\\ 1 & \text{circular polarization,}\end{cases} \quad (4)$$

where ψ is the phase of the particle in the laser field at the instant of ionization, $\tilde{a}$ is the normalized vector potential at the instant of ionization, and a is the laser envelope as defined above. The angle brackets emphasize that the oscillatory part of the solution has not been given. The transverse drift averages to zero when integrated over all particles, but the longitudinal drift does not. This implies that longitudinal momentum is constantly added to the electron fluid in the region of the ionization front. As shown in Ref. [11], the effective force density associated with this process is

$$nF=\left\langle\frac{d}{dt}np_\parallel\right\rangle\approx c\frac{dn}{dz}\langle p_\parallel\rangle. \quad (5)$$

This resembles a ponderomotive force in the sense that it is expressed in terms of a gradient, it depends on intensity, and it emerges out of an average over optical cycles. An explicit formula for the wake-field amplitude in the presence of this effect has been given in Ref. [12].

To understand ionization-induced steepening, consider the standard quasiparaxial wave equation for the laser envelope a,

$$(\nabla_T^2-2i\omega_0\partial_\tau+2\partial_{\tau\zeta})a=\frac{n}{\gamma}a,$$

where ∇_T^2 is the transverse Laplacian, $\tau=t$, γ is the relativistic Lorentz factor associated with a fluid element, and a system of units has been used where $c=\omega_p=1$. In one dimension, after expanding in the small parameters $1/\omega_0$ and a, this becomes

$$\partial_\tau a\approx-\frac{1}{2i\omega_0}\left(1+\frac{\partial_\zeta}{i\omega_0}\right)\left[na\left(1-\frac{|a|^2}{2}\right)\right].$$

By inserting the form $a=Ae^{i\theta}$, one obtains equations for the real-valued amplitude and phase

$$\frac{\partial A}{\partial\tau}=\frac{1}{2\omega_0^2}\left[A\left(1-\frac{A^2}{2}\right)\frac{\partial n}{\partial\zeta}+n\left(1-\frac{3A^2}{2}\right)\frac{\partial A}{\partial\zeta}\right],$$

$$\frac{\partial\theta}{\partial\tau}=\frac{n}{2\omega_0}\left(1-\frac{A^2}{2}\right)\left(1+\frac{1}{\omega_0}\frac{\partial\theta}{\partial\zeta}\right).$$

Inspection of the equation for A reveals that if $\partial n/\partial\zeta$ is large and negative, $\partial A/\partial\tau$ will be large and negative also. Since in the vicinity of an ionization front $\partial n/\partial\zeta$ is indeed large and negative, the laser amplitude will rapidly diminish there. Over time this will lead to the development of a depression in the laser envelope, which in turn implies the development of a steep gradient in laser intensity. The steepening of the laser envelope will lead to an enhanced ponderomotive impulse since the ponderomotive force is proportional to the gradient in laser intensity. This ponderomotive impulse will drive a wake field.

Physically, the reduction of the laser amplitude near the ionization front can be understood in terms of photons dispersing spatially due to the fact that photons in the plasma propagate more slowly than photons in vacuum.

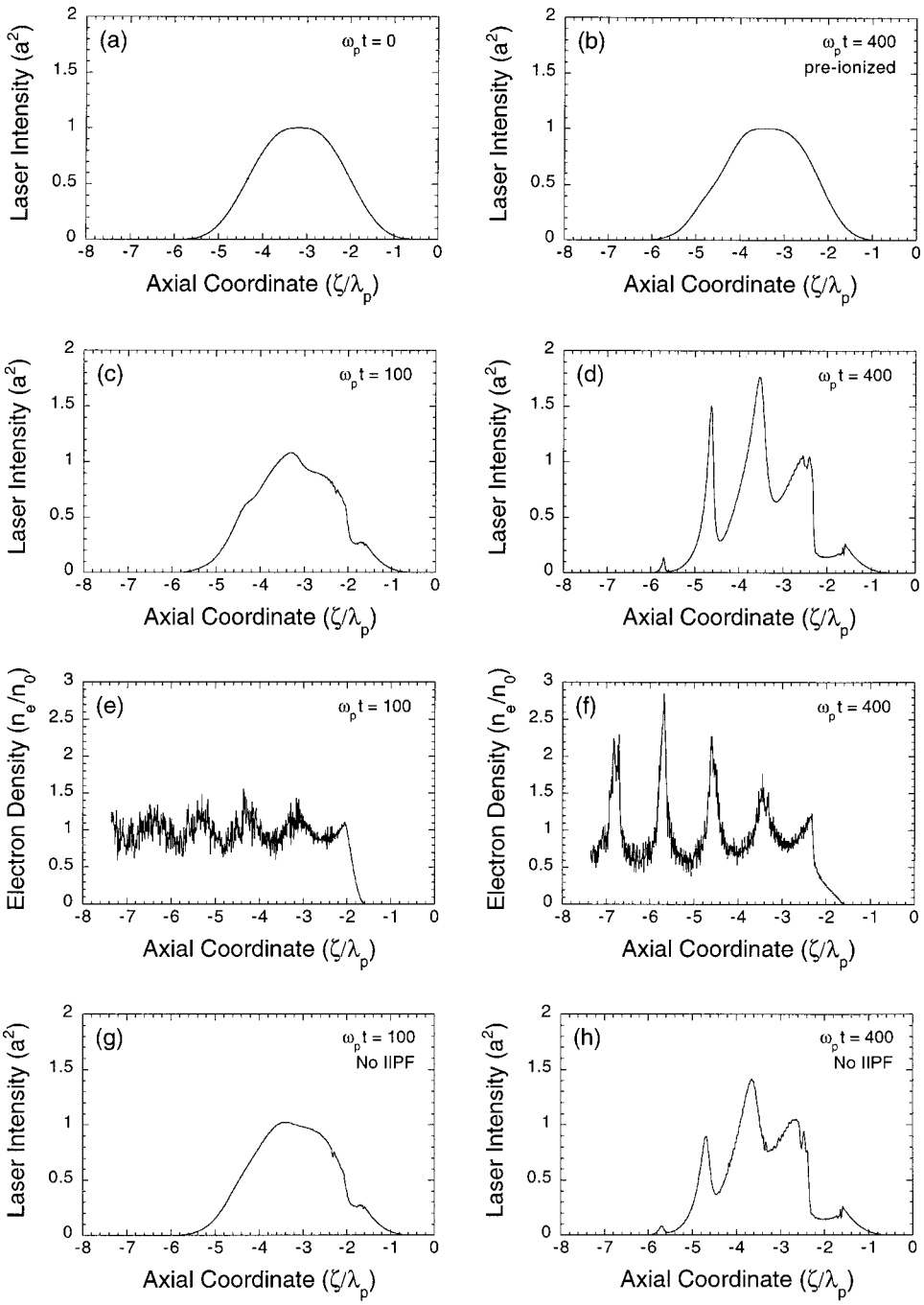

FIG. 1. Evolution of laser intensity in an illustrative regime. (a) Initial laser intensity. (b) Laser intensity after $400\omega_p^{-1}$ in preionized plasma. (c) Laser intensity after $100\omega_p^{-1}$ in hydrogen and (d) after $400\omega_p^{-1}$. (e) Electron density after $100\omega_p^{-1}$ in hydrogen and (f) after $400\omega_p^{-1}$. (g) Laser intensity after $100\omega_p^{-1}$ in hydrogen with the ionization-induced ponderomotive force turned off and (h) after $400\omega_p^{-1}$. Here, $\lambda_p = 2\pi c/\omega_p$. Intensity is plotted as the square of the normalized vector potential, a.

IV. SIMULATIONS

We model ionization effects in the self-modulated regime using turboWAVE, a fully relativistic, fully electromagnetic particle-in-cell (PIC) code [18]. TurboWAVE offers two modes of operation. First, it can be run as a standard fully explicit PIC code. Second, it can be run using the ponderomotive guiding center (PGC) algorithm [18]. Short descriptions of the the PGC algorithm and the ionization algorithm are given in the Appendixes. In the context of this paper, the distinction between the PGC mode and the fully explicit mode is primarily that the PGC algorithm does not account for RBS. This property is useful because it allows the effects of ionization to be isolated from the effects of RBS. We will perform simulations using both the PGC algorithm and the fully explicit algorithm. We will consider only circular polarization in order to keep the ionization rate constant on the optical time scale.

A. Illustration of ionization effects

We consider first a regime which is useful for illustrative purposes. From a pure plasma physics point of view, the regime of interest is defined by the peak vector potential $a_0 = 1$, the frequency ratio $\omega_0/\omega_p = 10$, and the pulse length $c\tau_{\text{pulse}} > \lambda_p$. If these quantities are regarded as fixed, the position of the ionization front within the laser pulse is determined by the type of gas and the laser frequency in physi-

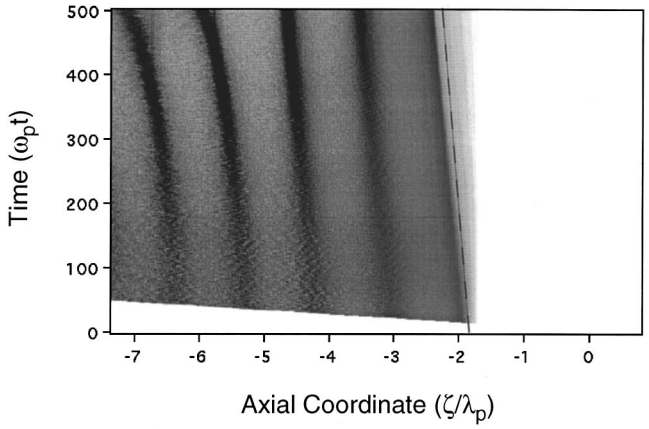

FIG. 2. Gray-scale image of the electron density showing recession of the ionization front. The dark areas correspond to high density. The dashed line represents the group velocity.

cal units. For purposes of illustration, it is most advantageous when the ionization front appears about half way up the rise time of the laser pulse. In the self-modulated regime, taking the case of hydrogen, this occurs for laser radiation with a wavelength of 75 μm and a gas density of 2×10^{15} cm^{-3}. The intensity of the laser would be on the order of 10^{14} W/cm^2. Again, these parameters are considered for illustrative purposes only. The more realistic case of 1 μm radiation will be dealt with below.

Figures 1(a) and 1(b) show the results of a simulation using the PGC algorithm where a circularly polarized laser pulse was propagated into a preionized plasma. The parameters are $a_0=1/\sqrt{2}$, $\omega_0=10\omega_p$, and $\tau_{\rm pulse}=20\omega_p^{-1}$, where $\tau_{\rm pulse}$ is the full width at half maximum and the pulse shape is the one discussed in Ref. [18]. The cell size was $0.05c/\omega_p$ and the time step was $0.025\omega_p^{-1}$. Each cell contained 40 simulation particles. The plasma-vacuum interface occupied one cell, and was placed $25c/\omega_p$ from the initial peak of the pulse. The figure shows that in the case of preionization, there is very little effect on the laser pulse after $400\omega_p^{-1}$ of propagation time.

Figures 1(c) through 1(f) show the results of a PGC simulation where a laser pulse was propagated into hydrogen gas. The parameters are the same as for the preionized case. The effect of ionization is dramatic. After only $100\omega_p^{-1}$ a significant modulation can be seen on the laser pulse. Ionization-induced steepening can also be observed. Figures 1(e) and 1(f) show the electron density. Initially, the electrons are loaded uniformly. However, the ionization process results in electron heating [19] which randomizes the electron positions over time. Thus, the noise level increases with distance behind the ionization front.

Figures 1(g) and 1(h) show the results of a simulation using the same parameters again, but with the ionization-induced ponderomotive force turned off. The modulation to the laser is smaller but still significant. Evidently, for these parameters, ionization-induced steepening and the ionization-induced ponderomotive force contribute about equally to the seeding of forward Raman.

Another interesting effect of ionization-induced steepening is that it causes the ionization front to recede in the group velocity frame of the laser. This can be understood in terms of the fact that as the laser amplitude is diminished, it eventually drops below the threshold for ionization. The ionization front must then move backwards to where the intensity is higher. Over time, therefore, the laser pulse develops a flat plateau in the region preceding the ionization front. This plateau can be seen in Figs. 1(c) and 1(d). Figure 2 illustrates the recession of the ionization front explicitly.

B. Ionization in the experimental regime

We next consider the experimental regime, defined by a laser wavelength of 1 μm. For the nominal SM-LWFA pa-

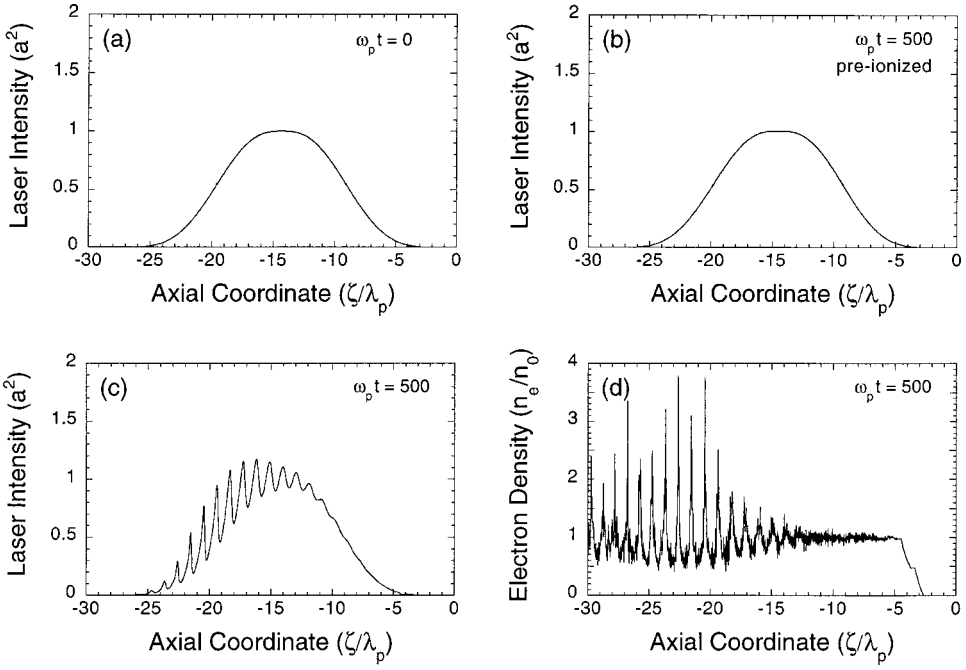

FIG. 3. PGC simulation of experimental SM-LWFA parameters. (a) Initial pulse. (b) Laser intensity in preionized plasma after $500\omega_p^{-1}$. (c) Laser intensity in helium after $500\omega_p^{-1}$. (d) Electron density in helium after $500\omega_p^{-1}$, showing He I and He II ionization fronts. Here, $\lambda_p=2\pi c/\omega_p$, and $E_{br}=mc\omega_p/e$ is the cold wave-breaking field. Intensity is plotted as the square of the normalized vector potential, a.

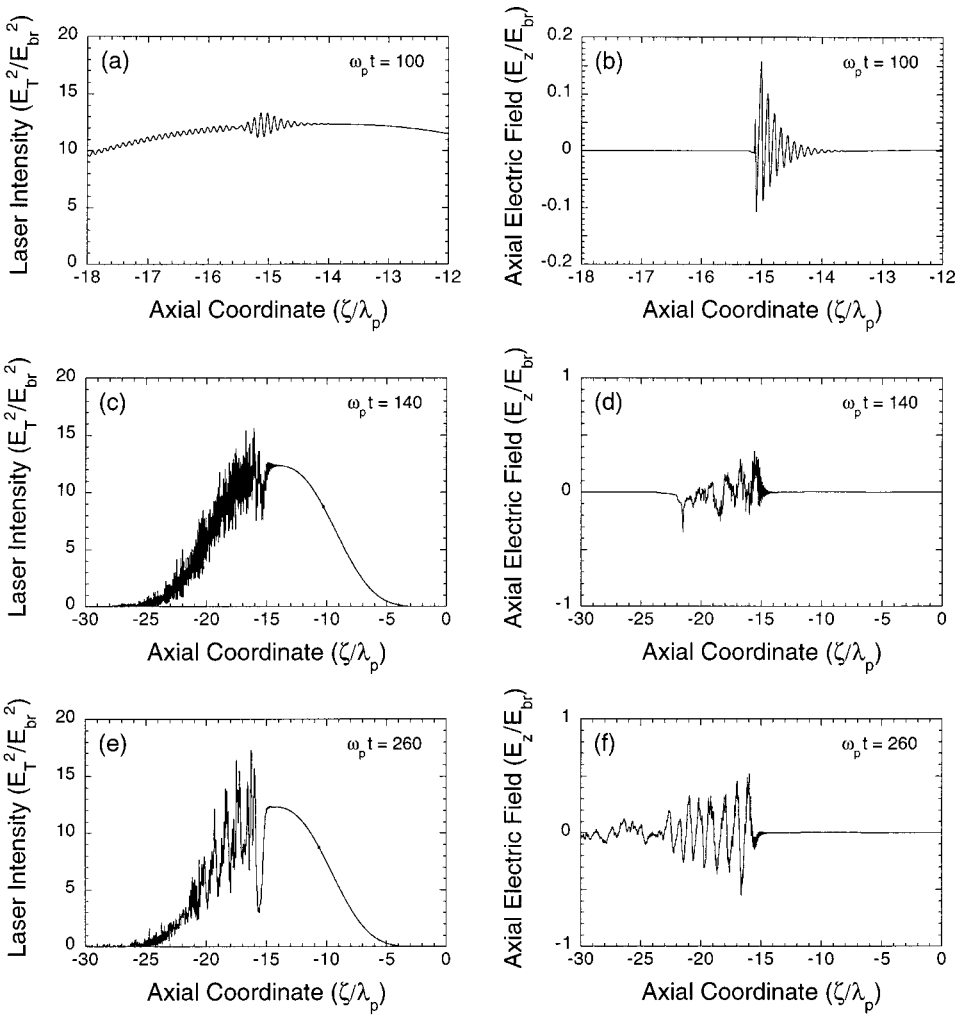

FIG. 4. Fully explicit PIC simulation of RBS and RFS in a preionized plasma. (a) Laser intensity after $100\omega_p^{-1}$, showing the onset of RBS. (b) Axial electric field after $100\omega_p^{-1}$. (c) Laser intensity after $140\omega_p^{-1}$, showing the early stages of RFS. (d) Axial electric field after $140\omega_p^{-1}$. (e) Laser intensity after $260\omega_p^{-1}$, showing the advanced stages of RFS. (f) Axial electric field after $260\omega_p^{-1}$. Here, E_T is the transverse electric field and $E_{br}=mc\omega_p/e$ is the cold wave-breaking field.

rameters considered in this paper, this corresponds to a plasma density of approximately $10^{19}\,\mathrm{cm}^{-3}$ and an intensity on the order of 10^{18} W/cm^2. For these parameters, the ionization front appears much earlier in the pulse than in the case of the illustrative regime. Nevertheless, ionization effects have a significant effect on the interaction.

We first consider PGC simulations with $a_0=1/\sqrt{2}$, $\omega_0=10\omega_p$, and $\tau_{\mathrm{pulse}}=90\omega_p^{-1}$. The laser is again circularly polarized, and starts out with its peak $95c/\omega_p$ from a one-cell-thick vacuum-plasma (or vacuum-gas) interface. The cell size was $0.1c/\omega_p$, the time step was $0.05\omega_p^{-1}$, and there were 40 particles per cell. Figures 3(a) and 3(b) show the outcome in the preionized case. After $500\omega_p^{-1}$ of propagation time, the modulation of the laser intensity is hardly perceptible. Figure 3(c) shows the laser intensity after $500\omega_p^{-1}$ of propagation time in helium. In this case the modulation is large. Figure 3(d) shows the electron density. Note the two ionization fronts associated with the two helium charge states. Comparison with Fig. 3(c) reveals that even the He II ionization front appears quite early in the laser pulse. This emphasizes the fact that small effects can strongly influence the outcome of a laser plasma interaction in the self-modulated regime.

C. Backscatter in the experimental regime

We now consider fully explicit PIC calculations. These calculations are distinguished from PGC calculations primarily in that they account for RBS. Although RBS saturates at a low level, it has a large growth rate and could be important in terms of its ability to seed RFS. Indeed, previous PIC simulations [10] have suggested that RBS causes a deformation of the pump wave form which generates a wake and causes RFS to appear earlier than would otherwise be expected.

In the simulations presented here, particles were loaded uniformly with zero thermal velocity. The seed for RBS was therefore as small as it could be made in a PIC code, arising either from round-off error, errors associated with the finite grid, or the physical mechanism discussed in Sec. II. It was confirmed that round-off error contributes to the noise source for RBS by noting that RBS started much earlier when lower precision floating point numbers were used for the calculation.

To determine the importance of RBS alone, we consider first a fully explicit PIC simulation where a circularly polarized laser with $a_0=1/\sqrt{2}$, $\omega_0=5\omega_p$, and $\tau_{\mathrm{pulse}}=90\omega_p^{-1}$ interacts with a preionized plasma. The cell size was

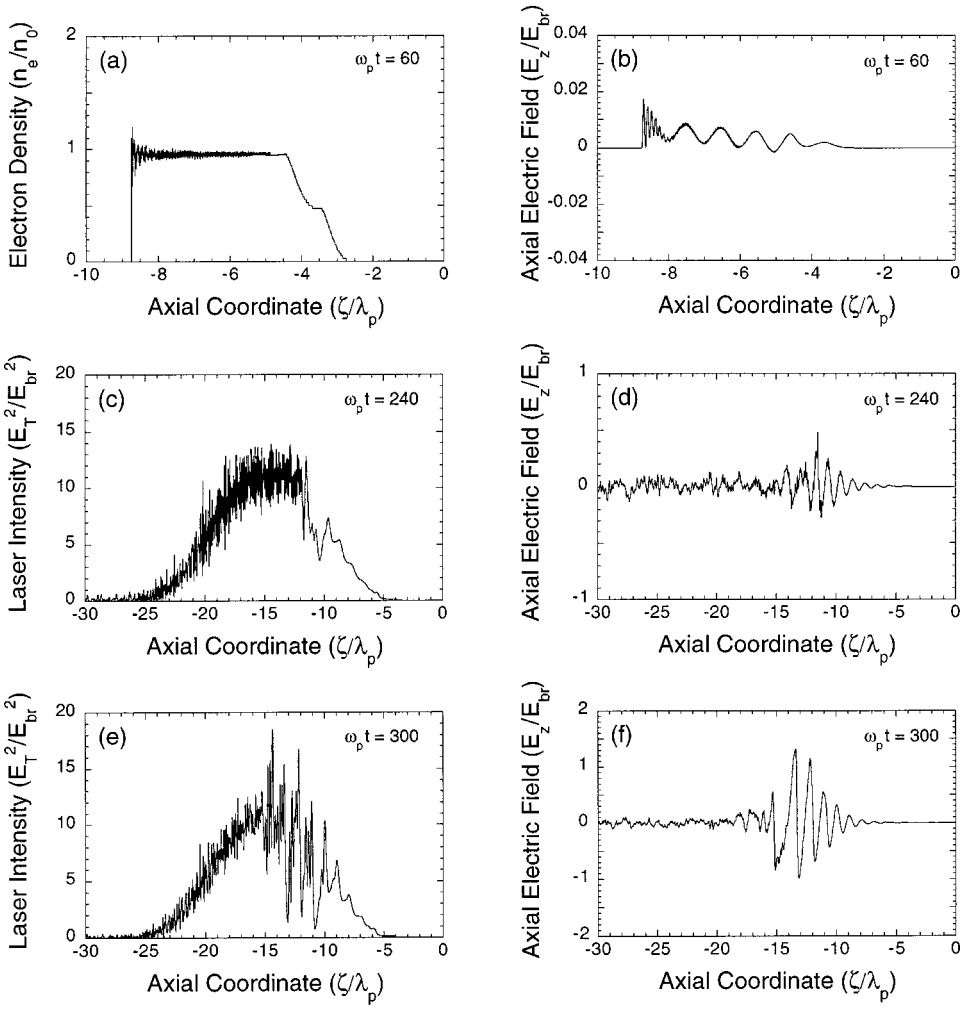

FIG. 5. Fully explicit PIC simulation of RBS and RFS in helium. (a) Electron density after $60\omega_p^{-1}$. (b) Axial electric field after $60\omega_p^{-1}$. (c) Laser intensity after $240\omega_p^{-1}$. (d) Axial electric field after $240\omega_p^{-1}$. (e) Laser intensity field after $300\omega_p^{-1}$. (f) Axial electric field after $300\omega_p^{-1}$. Here, E_T is the transverse electric field and $E_{br}=mc\omega_p/e$ is the cold wave-breaking field.

$0.025c/\omega_p$, the time step was $0.02\omega_p^{-1}$, and there were 40 particles per cell. Figure 4(a) shows the laser intensity after $100\omega_p^{-1}$. The prominent feature near the peak of the pulse has a wavelength of $0.11\lambda_p \approx 2\pi/2k_0 - k_p$, and can therefore be identified with the onset of RBS. The lower-level interference pattern behind the main feature is the reflection generated at the vacuum-plasma boundary. Figure 4(b) shows the axial electric field after $100\omega_p^{-1}$. The exponentially growing wave is again indicative of RBS. Figure 4(c) shows the laser intensity after $140\omega_p^{-1}$. A ''notch'' in the laser envelope has developed near the peak of the pulse, presumably due to continual depletion of the pump by the backward-propagating Stokes wave. This notch corresponds to the deformation that previous workers [10] identified as a seeding mechanism for forward Raman. This identification is consistent with Fig. 4(d), which shows a plasma wave with wave number $\approx \omega_p/c$ beginning to develop. Figures 4(e) and 4(f) show the laser intensity and axial electric field after $260\omega_p^{-1}$ of propagation time. The laser intensity is now modulated at the frequency associated with RFS, but the modulation is obscured by the finer structure imposed by RBS. The modulation associated with RFS can be more clearly seen in the axial electric field. Examination of Fig. 4(f) shows that the modulation peaks where it starts and decays toward the back of the pulse. This is the opposite of the behavior observed in the PGC simulations of Fig. 3. Apparently RBS generates a very strong noise source which is localized to the point in the pulse where RBS begins.

D. Backscatter and ionization together

For the last simulation, we consider the ionization of helium by a circularly polarized laser pulse with $a_0=1/\sqrt{2}$, $\omega_0=5\omega_p$, and $\tau_{\text{pulse}}=90\omega_p^{-1}$. The results are shown in Fig. 5. Figures 5(a) and 5(b) illustrate the onset of RBS, which occurs after about $60\omega_p^{-1}$ of propagation time. Careful inspection of Figs. 5(a) and 5(b) reveals that the wake starts at the location of the He I ionization front, and becomes more noticeable at the location of the He II ionization front. Figure 5(b) shows the high frequency wave associated with RBS developing a few wavelengths from the onset of the wake. The location of this feature was found to be weakly dependent on the number of particles used in the simulation. The onset of RBS was also studied using fluid simulations [15]. In fluid simulations with circular polarization and ionization, RBS arose in a manner very similar to that observed in Fig. 5.

The evolution of RFS is illustrated in Figs. 5(c) through 5(f). Figure 5(c) shows the laser intensity after $240\omega_p^{-1}$. This illustrates the early stages of RFS. The RBS notch can be

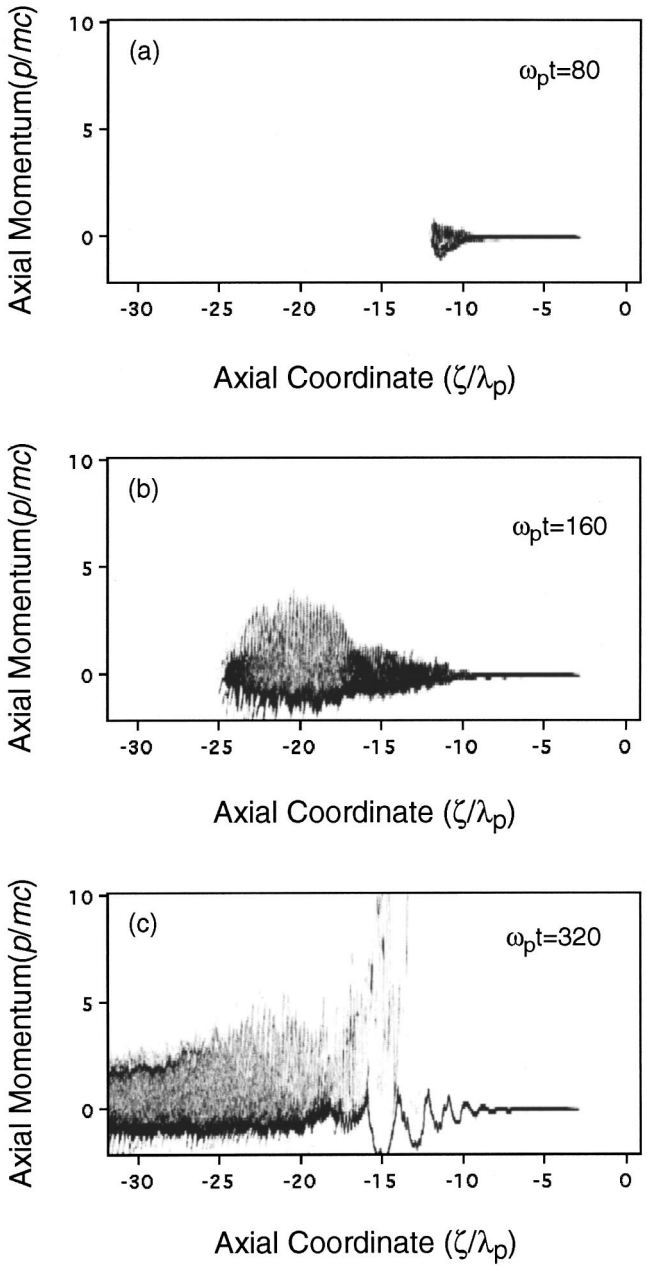

FIG. 6. Intensity plot of electron density in the ζ-p_z phase plane. (a) Phase-space density after $80\omega_p^{-1}$, (b) after $160\omega_p^{-1}$, and (c) after $320\omega_p^{-1}$.

seen near $\zeta=-10$. Figure 5(e) shows the laser intensity after $300\omega_p^{-1}$. At this point two distinct manifestations of RFS can be seen. For $\zeta<-10$, RFS is strongly affected by RBS. As discussed below, this involves the wave-breaking of RBS which heats the plasma very early in the interaction. The wave breaking of RFS also occurs, as evidenced by the fact that the axial electric field has exceeded the wave-breaking amplitude. For $\zeta>-10$, the instability is seeded only by ionization and occurs in a cold plasma. Correspondingly, the peaks in the laser intensity are cleanly separated by the plasma wavelength.

Finally, Fig. 6 shows the axial electron distribution function (EDF) at three times. Figure 6(a) shows the EDF after $80\omega_p^{-1}$. Substantial broadening has occurred in the region near $\zeta=-10$. Figure 6(b) shows the EDF after $160\omega_p^{-1}$. The hot electrons near $\zeta=-20$ are clear evidence of the wave breaking of RBS. Figure 6(c) shows the EDF after $320\omega_p^{-1}$. For $\zeta>-10$, the plasma is cold, but it also exhibits a modulation at the plasma wavelength due to RFS. The presence of very fast electrons near $\zeta=-15$ indicates the wave breaking of RFS in that region. The plasma continues to be heated by RBS for $\zeta<-15$.

V. CONCLUSIONS

Ionization fronts excite plasma waves because of the ionization-induced ponderomotive force and ionization-induced steepening. These plasma waves are an important seeding mechanism for the forward Raman instability, even in regimes where the ionization front appears very early in the pulse. If the noise source for backscatter could be made arbitrarily small, the ionization front would be the dominant seeding mechanism for typical SM-LWFA parameters. If backscatter grows to the point where significant pump depletion occurs, a deformation of the pump at the point in the pulse where RBS began also acts as a strong seed for forward Raman. This was indeed the case in PIC simulations where the noise source for RBS was reduced all the way to a level where round-off error was important.

When both ionization and backscatter are included in the same simulation, two distinct manifestations of RFS can be observed. In the region of the pulse unaffected by RBS, RFS causes a smooth modulation at the plasma frequency. In the region where RFS and RBS must coexist, the modulation is much less coherent.

ACKNOWLEDGMENTS

The authors would like to acknowledge useful conversations with A. Ting and C. I. Moore. This work was supported by the Office of Naval Research and the Department of Energy. D.F.G. is supported by the National Research Council.

APPENDIX A

In this appendix we give a brief description of the ponderomotive guiding center (PGC) algorithm. The PGC algorithm presumes there is a large separation between the frequency of the plasma response and the frequency of the laser fields. The plasma response is computed using standard PIC techniques. The calculation is fully electromagnetic and fully relativistic. The laser fields are computed according to an envelope equation for the complex-valued vector potential a defined by

$$a=\frac{\tilde{a}}{2}e^{i\omega(t-z)}+\text{c.c.},$$

where we have taken $c=1$. Using the speed of light variables $\zeta=z-t$ and $\tau=t$, it was shown by Mora and Antonsen, Jr. [20] that the envelope equation is approximated by

$$(-2i\omega_0\partial_\tau + 2\partial_{\tau\zeta} + \Delta_T)a = n_e\left\langle\frac{1}{\gamma}\right\rangle a,$$

where ω_0 is the laser frequency, Δ_T is the transverse Laplacian, and n_e is the slowly varying part of the electron density. Also, we define

$$\left\langle\frac{1}{\gamma}\right\rangle \equiv (1+P^2+|a|^2/2)^{-1/2},$$

where P is the slowly varying part of the momentum. Further, we have taken the plasma frequency, electronic mass, and magnitude of the electronic charge to be unity.

Once the fields are computed the electrons are pushed according to

$$\partial_t \mathbf{P} = -(\mathbf{E}+\mathbf{v}\times\mathbf{B}) - \left\langle\frac{1}{\gamma}\right\rangle \nabla\frac{|a|^2}{4},$$

where **E** and **B** are the slowly varying electric and magnetic fields associated with the wake. Finally, the charge density and current density are deposited onto the numerical grid for the solution of Maxwell's equations, while the quantity $\langle 1/\gamma\rangle$ is deposited onto the numerical grid for the solution of the envelope equation.

APPENDIX B

In this appendix we give a brief description of the turboWAVE ionization algorithm. The algorithm begins with a calculation of the ionization rate from Eq. (1). This is done by defining as a grid quantity the density of each neutral or ion species. The number of particles created in each cell during one time step is then computed. The fractional part is saved so that it can be added in during the next cycle. In the case of the explicit code, the new particles are added to the particle list with zero momentum. Spatially, they are loaded in the cell starting from the left and moving to the right at regular intervals. In the case of the PGC algorithm, the initial momentum is computed from Eqs. (3) and (4). In this case, the ionization-induced ponderomotive force can be ''turned off'' by loading the particles with zero momentum instead. Finally, the density corresponding to the number of particles added to the cell is subtracted from the neutral or ion density in the cell.

The above algorithm does not maintain the energy balance between the electromagnetic field and the ionization potential. However, in the regime we are considering this error is not serious. To fully ionize a cylinder of helium with radius 10 μm and length 500 μm requires about 25 μJ. The laser pulse contains about 1 J.

[1] W. B. Mori, IEEE J. Quantum Electron. **33**, 1942 (1997).

[2] A. Modena, Z. Najmudin, A. E. Dangor, C. E. Clayton, K. A. Marsh, C. Joshi, V. Malka, C. B. Darrow, C. Danson, D. Neely, and F. N. Walsh, Nature (London) **377**, 606 (1995).

[3] C. I. Moore, A. Ting, K. Krushelnick, E. Esarey, R. F. Hubbard, B. Hafizi, H. R. Burris, C. Manka, and P. Sprangle, Phys. Rev. Lett. **79**, 3909 (1997).

[4] E. Esarey, B. Hafizi, R. Hubbard, and A. Ting, Phys. Rev. Lett. **80**, 5552 (1998).

[5] A. Ting, C. I. Moore, K. Krushelnick, C. Manka, E. Esarey, P. Sprangle, R. Hubbard, H. R. Burris, R. Fischer, and M. Baine, Phys. Plasmas **4**, 1889 (1997).

[6] R. Wagner, S.-Y. Chen, A. Maksimchuk, and D. Umstadter, Phys. Rev. Lett. **78**, 3125 (1997).

[7] K.-C. Tzeng, W. B. Mori, and T. Katsouleas, Phys. Rev. Lett. **79**, 5258 (1997).

[8] D. Gordon, K.-C. Tzeng, C. E. Clayton, A. E. Dangor, V. Malka, K. A. Marsh, A. Modena, W. B. Mori, P. Muggli, Z. Najmudin, D. Neely, C. Danson, and C. Joshi, Phys. Rev. Lett. **80**, 2133 (1998).

[9] C. Gahn, G. D. Tsakiris, A. Pukhov, J. Meyer-ter-Vehn, G. Pretzler, P. Thirolf, D. Habs, and K. J. Witte, Phys. Rev. Lett. **83**, 4772 (1999).

[10] C. D. Decker, W. B. Mori, and T. Katsouleas, Phys. Rev. E **50**, 3338 (1994).

[11] W. B. Mori and T. Katsouleas, Phys. Rev. Lett. **69**, 3495 (1992).

[12] N. E. Andreev, M. E. Veisman, M. G. Cadjan, and M. V. Chegotov, Plasma Phys. Rep. **26**, 947 (2000).

[13] S. P. Leblanc, M. C. Downer, R. Wagner, S.-Y. Chen, A. Maksimchuk, G. Mourou, and D. Umstadter, Phys. Rev. Lett. **77**, 5381 (1996).

[14] D. W. Forslund, J. M. Kindel, and E. L. Lindman, Phys. Fluids **18**, 1002 (1975).

[15] The fluid code will be described in a future publication.

[16] M. V. Ammosov, N. B. Delone, and V. P. Krainov, Zh. Eksp. Teor. Fiz. **91**, 2008 (1986) [Sov. Phys. JETP **64**, 1191 (1986)].

[17] E. Esarey, P. Sprangle, J. Krall, and A. Ting, IEEE Trans. Plasma Sci. **24**, 252 (1996).

[18] D. F. Gordon, W. B. Mori, and T. M. Antonsen, Jr., IEEE Trans. Plasma Sci. **28**, 1224 (2000).

[19] P. B. Corkum, N. H. Burnett, and F. Brunel, Phys. Rev. Lett. **62**, 1259 (1989).

[20] P. Mora and T. Antonsen, Phys. Plasmas **4**, 217 (1997).